Observation of Ion Acceleration and Heating during Collisionless Magnetic Reconnection in a Laboratory Plasma

Jongsoo Yoo,* Masaaki Yamada, Hantao Ji, and Clayton E. Myers
Center for Magnetic Self-organization in Laboratory and Astrophysical Plasmas, Princeton Plasma Physics Laboratory, Princeton, New Jersey 08543, USA
(Received 6 December 2012; published 24 May 2013)

The ion dynamics in a collisionless magnetic reconnection layer are studied in a laboratory plasma. The measured in-plane plasma potential profile, which is established by electrons accelerated around the electron diffusion region, shows a saddle-shaped structure that is wider and deeper towards the outflow direction. This potential structure ballistically accelerates ions near the separatrices toward the outflow direction. Ions are heated as they travel into the high-pressure downstream region.

DOI: 10.1103/PhysRevLett.110.215007 PACS numbers: 52.35.Vd, 52.30.−q

Magnetic reconnection is a fundamental process in magnetized plasma in which magnetic energy is converted to particle energy through the topological rearrangement of magnetic field lines. In recent studies of collisionless magnetic reconnection, progress has been made in understanding the dynamics of electrons and ions in the context of two-fluid dynamics [1], which result from the different behaviors of large orbit ions and small orbit magnetized electrons, leading to a strong Hall effect. In collisionless plasmas, this Hall effect facilitates a faster reconnection than that predicted by the classical Sweet-Parker rate [2,3]. However, the mechanisms that convert magnetic energy to particle energy during reconnection are not well understood. This remains one of the foremost challenges in magnetic reconnection research.

Ion acceleration and heating during magnetic reconnection have been a focal point of research both experimentally [4–11] and computationally [12–15]. Additionally, in the magnetosphere, high-speed Alfvénic ion jets have been attributed to the reconnection outflow [16–18]. Despite all these efforts, it has not been resolved how ions are heated and/or accelerated, particularly in a collisionless reconnection layer.

In this Letter, we present measurements of the two-dimensional (2-D) in-plane potential profile together with measurements and analysis of ion acceleration and heating in the collisionless plasma of the Magnetic Reconnection Experiment (MRX) [19]. As seen in numerical simulations [20–22] and space observations [23], the potential well along the direction normal to the current sheet becomes deeper and broader downstream, creating a saddle-shaped potential profile in the reconnection plane. This unique in-plane potential is established by electron dynamics around the electron diffusion region (EDR). A large in-plane electric field ($|\mathbf{E}_{\rm in}| \sim 500$–$800$ V/m) over a short spatial scale ($< \delta_i \equiv c/\omega_{pi}$) ballistically accelerates ions up to a significant fraction (0.5) of the Alfvén velocity $V_A \equiv B_{\rm rec}/\sqrt{\mu_o \rho}$ near the separatrices. Here, $B_{\rm rec}$ is the reconnecting magnetic field. As ions travel into the high-pressure downstream region, energy from $\mathbf{E}_{\rm in}$ preferentially heats ions.

Figure 1(a) shows a cross section of the MRX device in the R-Z plane. The two gray circles are "flux cores" that each contain two independent coils: a poloidal field (PF) coil and a toroidal field (TF) coil. The PF coils generate the X-line geometry at the center of the MRX device and drive magnetic reconnection, whereas the TF coils inductively create the plasma around the flux cores. No external guide field is applied for this study so that the reconnecting field lines are nearly antiparallel during the quasisteady period

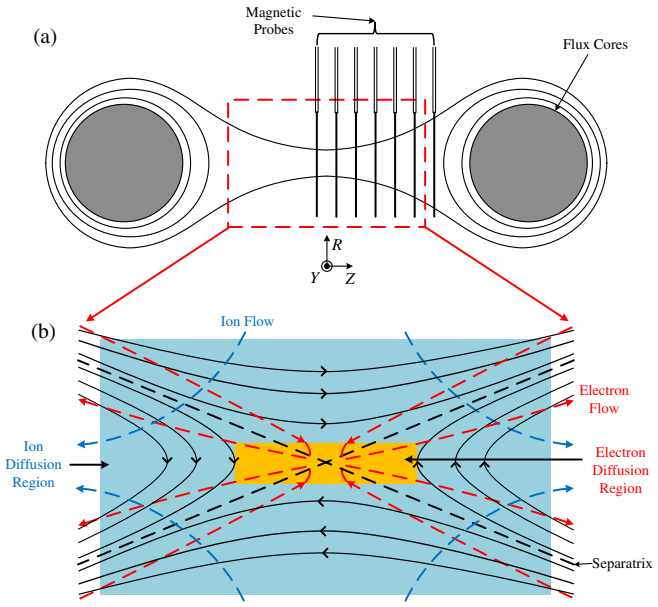

FIG. 1 (color online). (a) A cross section of MRX. The flux core contains the PF coil for driving magnetic reconnection and the TF coil for creating the plasma. Magnetic probes are inserted to monitor the evolution of the 2-D magnetic geometry. (b) Enlarged view of the reconnection layer marked by the dashed red box in (a). The EDR is embedded in the much larger IDR. The blue dashed lines illustrate typical ion flow, whereas the red lines show electron flow.

over which the reconnection rate is relatively constant. Figure 1(b) illustrates the detailed geometry of our measurement region. Due to the fundamental scale difference between electrons and ions, ions are decoupled from electrons in the ion diffusion region (IDR), which leads to strong Hall effects inside of the IDR.

Because of a relatively low electron temperature (≤ 12 eV) and short discharge duration (<1 ms), *in situ* measurements of plasma quantities are possible in MRX. In this experimental campaign, the evolution of all three components of the magnetic field is measured by a 2-D magnetic probe array with a maximum radial resolution of 0.6 cm and an axial spacing of 3 cm. The electron temperature and density are measured by triple Langmuir probes. A radial profile of the floating potential (Φ_f) is obtained by a 17-tip floating potential probe array with a maximum resolution of 0.7 cm. Local ion temperature and flow velocity are measured by ion dynamics spectroscopy probes (IDSPs) [24] by fitting He II 4686 Å spectra into a sum of 13 Gaussian functions to take fine structure effects into account [25]; otherwise, the ion temperature is overestimated by 15–25%. The signal from the IDSPs is recorded by a gated, intensified charge-coupled device camera. The time resolution of the IDSPs is limited by the gate-open time of 5.6 μs, and the spatial resolution is given by the distance between the lens and a view dump of 3–4 cm. Ion flow data are also obtained from Mach probes. Because of their better time and spatial resolution, the ion flow data measured by the Mach probes are presented. The Mach probe flow data are calibrated to corresponding IDSP flow measurements.

Using an extensive R-Z scan of the above probes, we obtain 2-D profiles of various plasma parameters such as electron density n_e, electron temperature T_e, ion temperature T_i, ion flow $\mathbf{V}_i$, and Φ_f. Among more than 4200 discharges, shots are scrutinized based on the reproducibility of data from magnetic probes and a reference Langmuir probe. To facilitate the ion temperature measurement, helium discharges with a fill pressure of 4.5 mT are used. Plasma parameters are controlled such that the plasma is in the collisionless regime during the quasisteady period. In this regime, the resistive term ($\eta_\perp J_Y$, where $\eta_\perp$ is perpendicular Spitzer resistivity) accounts for about 10% of the reconnection electric field (E_Y) at the X point. The mean free path of electrons at the X point is about 8–12 cm, which is larger than the measured current sheet half width of about 2 cm.

Figure 2(a) shows the measured 2-D profile of the plasma potential Φ_p in the middle of the quasisteady reconnection period along with contours of the poloidal flux $\Psi \equiv \int_0^R 2\pi R' B_Z dR'$. The plasma potential is obtained by measuring Φ_f and T_e and using the relation $\Phi_p \sim \Phi_f + (3.3 + 0.5\ln\mu)T_e$, where $\mu = m_i/m_p$ and T_e is in units of eV [26]. The red asterisks in Fig. 2(b) show the radial profile of Φ_p at $Z = 0$. The magnitude of the potential

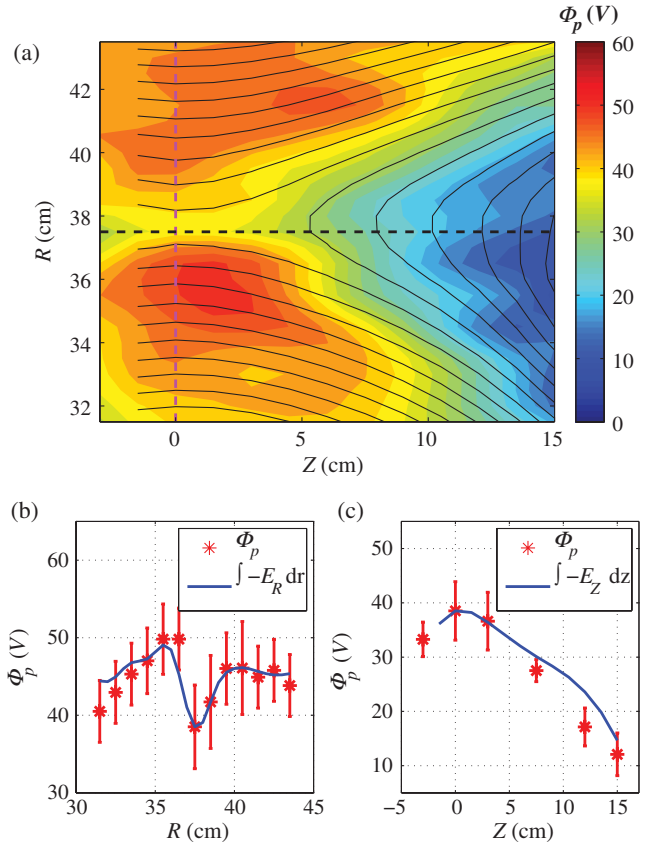

FIG. 2 (color). (a) Measured 2-D plasma potential profile with contours of the poloidal flux Ψ (black lines). The radial potential well becomes deeper and wider downstream. (b) Radial profile of Φ_p at $Z = 0$ [along the magenta dashed line in (a)]. The red asterisks are the measured Φ_p values, and the blue line is the radial integration of the right-hand side of Eq. (2). Two profiles are in agreement. (c) Axial profile of Φ_p at $R = 37.5$ cm [along the black dashed line in (a)]. The red asterisks are the measured Φ_p values, and the blue line comes from the integration of the right-hand side of Eq. (4) along Z.

well is about 10 V, and its half width is the same as the current sheet width. As shown in Fig. 2(c), the magnitude of the radial potential well becomes deeper downstream, reaching 35 V. It also becomes wider downstream as its boundary expands along the separatrices. These results are consistent with recent numerical simulations [20–22]. It is notable that the flux contours in Fig. 2(a) almost match the Φ_p contours, suggesting that Φ_p is relatively constant along magnetic field lines.

This in-plane potential profile is governed by electron dynamics around the EDR. The acceleration of electrons by E_Y around the EDR is the fundamental driving force of the Hall electric field. To test this hypothesis, let us write down the electron momentum equation [1]

$$n_e m_e \frac{d\mathbf{V}_e}{dt} = -en_e(\mathbf{E} + \mathbf{V}_e \times \mathbf{B}) - \nabla \cdot \overline{\mathbf{P}}_e + en_e \overline{\boldsymbol{\eta}} \cdot \mathbf{J}, \quad (1)$$

where $\overline{\mathbf{P}}_e$ is the electron pressure tensor and $\overline{\boldsymbol{\eta}}$ is the resistivity tensor. After the negligible electron inertial term and resistivity term are ignored and the pressure tensor is assumed to be isotropic, the R component of the above equation at $Z = 0$ leads to

$$E_R \approx -V_{eY}B_Z - \frac{1}{en_e}\frac{\partial p_e}{\partial R}. \quad (2)$$

Since both B_R and B_Y are small at $Z = 0$, the out-of-plane component of the electron diamagnetic drift V^*_{eY} can be approximated as $V^*_{eY} \equiv (\nabla p_e \times \mathbf{B})_Y/(en_eB^2) \approx -(1/en_eB_Z)\partial p_e/\partial R$. Then, Eq. (2) can be rewritten as

$$E_R \approx -(V_{eY} - V^*_{eY})B_Z. \quad (3)$$

The diamagnetic drift term is not negligible due to strong electron heating near the current sheet that cannot be explained by classical Ohmic heating [27]. The radial electric field reverses sign at the X point where the sign of B_Z also reverses. This indicates that the bipolar radial electric field is the result of electron force balance [28]. Since V_{eY} contains the diamagnetic component, Eq. (3) implies that the electron diamagnetic drift does not contribute to E_R; only pure acceleration by E_Y plays a role [29]. By integration of the right-hand side of Eq. (3) along R, the radial potential profile can be estimated. The electron flow velocity is obtained by $\mathbf{V}_e = -\mathbf{J}/en_e + \mathbf{V}_i = -\nabla \times \mathbf{B}/\mu_0 en_e + \mathbf{V}_i$. As shown in Fig. 2(b), the estimates by Eq. (3) (the blue line) agree with the measured values (red asterisks).

Similarly, the electron momentum equation along the outflow direction at $R = 37.5$ cm yields

$$E_Z \approx V_{eY}B_R - \frac{1}{en_e}\frac{\partial p_e}{\partial Z}. \quad (4)$$

As electrons flow out of the EDR with high V_{eY}, they create a further potential decrease along the outflow direction Z. The amount of the further potential decrease can be estimated by integrating Eq. (4) along Z, which agrees with the measured values as shown in Fig. 2(c). Because of the high mobility of electrons, the potential drop around the EDR is conveyed along magnetic field lines, creating a strong $\mathbf{E}_{\text{in}}$ near the separatrices as shown in Fig. 2(a).

The strong Hall electric field ballistically accelerates ions near the separatrices where the ions are unmagnetized. The magnitude of $\mathbf{E}_{\text{in}}$ near the boundary can exceed 700 V/m, which is much larger than E_Y (~ 200 V/m). Furthermore, its spatial scale is smaller than the ion skin depth $\delta_i = c/\omega_{pi}$ (~ 9 cm). Thus, as soon as the ions see the strong $\mathbf{E}_{\text{in}}$, they are accelerated toward the outflow direction. Figure 3(a) shows the ion flow vector profile measured by Mach probes along with contours of Φ_p. Considerable changes in the ion flow occur near the boundary. The corresponding large difference between

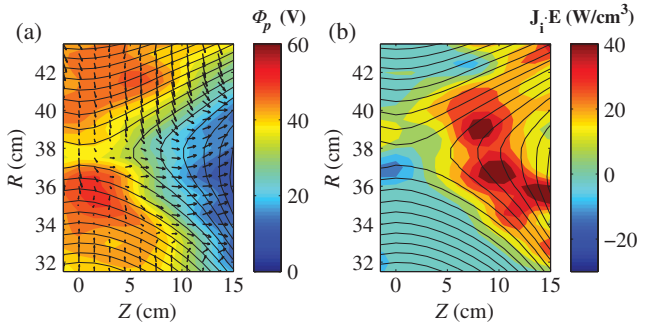

FIG. 3 (color). (a) In-plane ion flow vector measured by Mach probes together with contours of Φ_p and Ψ. The flow vectors are measured every 1 cm along R and every 3 cm along Z. The maximum ion velocity is 16 km/s. As ions flow across the separatrices, they are accelerated by $\mathbf{E}_{\text{in}}$ and turn into the outflow direction. (b) Work done by the electric field on ions per unit time and unit volume. It is dominated by the strong Hall field.

the ion and electron in-plane flow profiles produces the well-known quadrupole out-of-plane magnetic field [30]. It is worth noting that the stagnation point of the ion flow is shifted to the inboard side ($R < 37.5$), which is caused by the upstream density asymmetry [31]; the outboard side ($R > 37.5$) has about 2–3 times greater density than the inboard side due to radial symmetry-breaking processes in the earlier phases of the discharge [32].

Figure 3(b) shows the profile of the work done by the electric field on the ions per unit time and unit volume, $\mathbf{J}_i \cdot \mathbf{E}$. The in-plane electric field is calculated by $\mathbf{E}_{\text{in}} = -\nabla\Phi_p$, and the out-of-plane reconnection electric field is estimated by $E_Y = -(\partial\Psi/\partial t)/2\pi R$. The work done by E_Y is fairly uniform over the measurement region, which is inside of the IDR, with values of 2–8 W/cm^3. On the other hand, the work done by $\mathbf{E}_{\text{in}}$ is localized downstream with higher values of 20–50 W/cm^3. This means that ions gain energy mostly from the Hall electric field, which agrees with recent simulation results [22,33].

In addition to ion acceleration, we also observe ion heating downstream. Figure 4(a) shows measured He 4686 Å spectra at the X point [$(R, Z) = (37.5, 0)$, black asterisks] and downstream [$(R, Z) = (37.5, 15)$, green crosses]. Clear broadening (heating) and shifting (acceleration) exist in the spectrum at $Z = 15$ cm. Figure 4(b) shows the axial (Z) profile of T_i and V_{iZ} at $R = 37.5$ cm. The ion temperature starts to rise at $Z = 9$ cm where V_{iZ} begins to saturate. Finally, Fig. 4(c) shows a radial profile of T_i downstream at $Z = 15$ cm. The ion temperature is peaked at the center of the layer while V_{iZ} has a broader profile. These profiles suggest that ions are heated after they are accelerated by $\mathbf{E}_{\text{in}}$ near the separatrices.

The observed ion temperature profile cannot be explained by classical viscous heating in the unmagnetized limit [34]. The region where ions are heated does not match the area where classical viscous damping is strong (i.e., where strong velocity shear and/or acceleration exist).

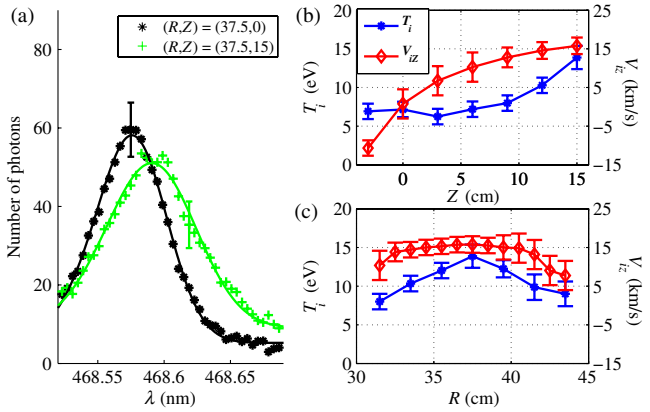

FIG. 4 (color online). (a) Spectra of He 4686 Å at $(R, Z) = (37.5, 0)$ (black asterisks) and at $(R, Z) = (37.5, 15)$ (green crosses). Refer to Fig. 2(a) for measurement locations. Solid lines are from fitting the spectra into the sum of 13 Gaussian functions. Both ion heating and acceleration are observed at $(R, Z) = (37.5, 15)$. (b) Axial T_i and V_{iZ} profiles at $R = 37.5$ cm. For $Z > 9$ cm, the ion temperature rises significantly while V_{iZ} begins to saturate. (c) Radial T_i and V_{iZ} profiles at $Z = 15$ cm (downstream). The ion temperature profile is peaked at the center of the layer whereas the outflow profile is broader.

Furthermore, heat conduction is too large to sustain the observed ion temperature gradient. This suggests that other heating mechanisms are responsible for the measured profiles.

One possible mechanism that can explain the observed downstream heating is the remagnetization of the ions in the outflow region. In particular, the influence of the magnetic field is not negligible away from the X point, especially further downstream ($Z > 12$ cm) where the magnetic field becomes strong enough to make the local ion gyroradius smaller than the local inertial length of 5–6 cm. In this case, the ion gyromotion can prolong the transit of the ions through the outflow region, significantly increasing the chance that ions are thermalized via collisions and/or scattered by wave-particle interactions. Additionally, the frictional drag caused by the high density downstream plasma may also play a role. Since the downstream plasma density ($5–8 \times 10^{13}$ cm^{-3}) is higher than the upstream density ($1–2.5 \times 10^{13}$ cm^{-3}), the local ion mean free path is reduced from 6–12 to 2–5 cm in the downstream region. Thus, as the ions travel further downstream, they lose energy to the ambient plasma through collisions—a process that generates heat. This mechanism differs from the aforementioned classical viscous heating mechanism because this process results from a beam-plasma interaction.

The heating could also result from other mechanisms such as kinetic effects from characteristic bouncing motion of ions inside of the potential well [14,15,33]. Boundary effects from existence of the flux cores may be also important. Detailed studies of the ion thermalization process in the downstream region will be conducted in the future via numerical simulations.

In summary, we have measured the 2-D in-plane potential profile together with the 2-D ion flow profile in a laboratory plasma. We have observed both ion acceleration and heating in the ion diffusion region and identified possible mechanisms to explain these observations. The in-plane electrostatic field is established by electron dynamics around the electron diffusion region. Ions are accelerated to $0.5V_A$ by the strong Hall electric field as they flow across the separatrices. As they travel into the high-pressure downstream region, ions are heated.

Further work is under way to address important questions related to general aspects of particle heating and acceleration during reconnection. Examples are the dependence of the energy conversion process on collisionality, the role of plasma β, and mechanisms for the measured anomalous electron heating in the current sheet. We will pursue these issues in our future research.

This work is supported by DOE and NSF. We thank J. Drake, M. Goldman, W. Daughton, and J. Jara-Almonte for valuable discussions, and R. Cutler for technical supports.

*jyoo@pppl.gov

[1] M. Yamada, R. Kulsrud, and H. Ji, Rev. Mod. Phys. **82**, 603 (2010).
[2] J. Birn *et al.*, J. Geophys. Res. **106**, 3715 (2001).
[3] M. Yamada, Y. Ren, H. Ji, J. Breslau, S. Gerhardt, R. Kulsrud, and A. Kuritsyn, Phys. Plasmas **13**, 052119 (2006).
[4] P. J. Baum and A. Bratenahl, J. Plasma Phys. **11**, 93 (1974).
[5] W. Gekelman, R. L. Stenzel, and N. Wild, J. Geophys. Res. **87**, 101 (1982).
[6] Y. Ono, M. Yamada, T. Akao, T. Tajima, and R. Matsumoto, Phys. Rev. Lett. **76**, 3328 (1996).
[7] S. C. Hsu, G. Fiksel, T. Carter, H. Ji, R. Kulsrud, and M. Yamada, Phys. Rev. Lett. **84**, 3859 (2000).
[8] M. R. Brown, C. D. Cothran, M. Landreman, D. Schlossberg, W. H. Matthaeus, G. Qin, V. S. Lukin, and T. Gray, Phys. Plasmas **9**, 2077 (2002).
[9] A. Stark, W. Fox, J. Egedal, O. Grulke, and T. Klinger, Phys. Rev. Lett. **95**, 235005 (2005).
[10] G. Fiksel, A. Almagri, B. Chapman, V. Mirnov, Y. Ren, J. Sarff, and P. Terry, Phys. Rev. Lett. **103**, 145002 (2009).
[11] Y. Ono, H. Tanabe, Y. Hayashi, T. Ii, Y. Narushima, T. Yamada, M. Inomoto, and C. Z. Cheng, Phys. Rev. Lett. **107**, 185001 (2011).
[12] M. Hoshino, T. Mukai, T. Yamamoto, and S. Kokubun, J. Geophys. Res. **103**, 4509 (1998).
[13] W. Pei, R. Horiuchi, and T. Sato, Phys. Rev. Lett. **87**, 235003 (2001).
[14] J. F. Drake, M. Swisdak, T. D. Phan, P. A. Cassak, M. A. Shay, S. T. Lepri, R. P. Lin, E. Quataert, and T. H. Zurbuchen, J. Geophys. Res. **114**, A05111 (2009).
[15] N. Aunai, G. Belmont, and R. Smets, J. Geophys. Res. **116**, A09232 (2011).
[16] G. Paschmann, B. U. Ö. Sonnerup, I. Papamastorakis, N. Sckopke, G. Haerendel, S. J. Bame, J. R. Asbridge, J. T.

Gosling, C. T. Russell, and R. C. Elphic, Nature (London) **282**, 243 (1979).
[17] M. Øieroset, T. D. Phan, M. Fujimoto, R. P. Lin, and R. P. Lepping, Nature (London) **412**, 414 (2001).
[18] T. D. Phan *et al.*, Nature (London) **439**, 175 (2006).
[19] M. Yamada, H. Ji, S. Hsu, T. Carter, R. Kulsrud, N. Bretz, F. Jobes, Y. Ono, and F. Perkins, Phys. Plasmas **4**, 1936 (1997).
[20] H. Karimabadi, W. Daughton, and J. Scudder, Geophys. Res. Lett. **34**, L13104 (2007).
[21] J. F. Drake, M. A. Shay, and M. Swisdak, Phys. Plasmas **15**, 042306 (2008).
[22] P. L. Pritchett, J. Geophys. Res. **115**, A10208 (2010).
[23] J. R. Wygant *et al.*, J. Geophys. Res. **110**, A09206 (2005).
[24] G. Fiksel, D. J. D. Hartog, and P. W. Fontana, Rev. Sci. Instrum. **69**, 2024 (1998).
[25] W. L. Wiese and J. R. Fuhr, J. Phys. Chem. Ref. Data **38**, 565 (2009).
[26] The effect from the finite ion temperature is negligible as long as $T_i < 2T_e$, which is well satisfied in the MRX discharge. See, e.g., Fig. 9 in I. H. Hutchinson, Plasma Phys. Controlled Fusion **44**, 1953 (2002).
[27] H. Ji, S. Terry, M. Yamada, R. Kulsrud, A. Kuritsyn, and Y. Ren, Phys. Rev. Lett. **92**, 115001 (2004).
[28] B. Li and R. Horiuchi, Phys. Rev. Lett. **101**, 215001 (2008).
[29] D. A. Uzdensky and R. M. Kulsrud, Phys. Plasmas **13**, 062305 (2006).
[30] Y. Ren, M. Yamada, H. Ji, S. P. Gerhardt, and R. Kulsrud, Phys. Rev. Lett. **101**, 085003 (2008).
[31] P. A. Cassak and M. A. Shay, Phys. Plasmas **14**, 102114 (2007).
[32] M. Inomoto, S. Gerhardt, M. Yamada, H. Ji, E. Belova, A. Kuritsyn, and Y. Ren, Phys. Rev. Lett. **97**, 135002 (2006).
[33] M. V. Goldman *et al.*, presented at *the 54th Annual APS-DPP Meeting, Providence, RI, 2012.*
[34] S. I. Braginskii, in *Reviews of Plasma Physics*, edited by M. A. Leontovich (Consultants Bureau, New York, 1965), Vol. 1, pp. 205–311.